PROCEEDINGS A

royalsocietypublishing.org/rspa

CC BY

Research

Cite this article: Chantelot P, Croquette S, Lemoult F. 2026 Guided elastic waves informed material modelling of soft incompressible media. *Proc. R. Soc. A* **482**: 20260254.
https://doi.org/10.1098/rspa.2026.0254

Received: 23 March 2026
Accepted: 29 July 2026

Subject Category:
Physics

Subject Areas:
mechanics, wave motion

Keywords:
soft matter, acoustoelasticity, viscoelasticity, guided elastic waves

Author for correspondence:
Pierre Chantelot
e-mail: p.chantelot@gmail.com

Guided elastic waves informed material modelling of soft incompressible media

Pierre Chantelot, Samuel Croquette, Fabrice Lemoult

Institut Langevin, ESPCI Paris, Université PSL, CNRS, 75005 Paris, France

PC, 0000-0003-1342-2539

Identifying a universal material constitutive law which describes the mechanical response of rubber-like solids for all deformation fields and achievable extensions, is an outstanding challenge. Here, we propose to exploit the propagation of elastic waves and demonstrate that monitoring incremental guided wave propagation in an elastomer plate undergoing uniaxial extension reveals model sensitivities that are inaccessible in the corresponding static test. We measure the dispersion relations of the three zero-order guided modes propagating parallel and perpendicular to the direction of imposed elongation. We compare them with predictions from the acoustoelastic theory, which also takes into account material rheology, using parameters extracted from fitting the uniaxial stress–strain curve across three successive elongation regimes, following the methodical procedure of (Destrade *et al.* 2017 *Proc. R. Soc. A: Math. Phys. Eng. Sci.* **473**, 20160811. (doi:10.1098/rspa.2016.0811)). We evidence that our approach lifts the degeneracy between hyperelastic models with different functional forms of the so-called C_2 term, which remains indistinguishable from static uniaxial tension stress–strain measurements alone. However, like their static counterpart, our dynamic measurements cannot distinguish between different generalized neo-Hookean models.

1. Introduction

Natural rubber, synthetic elastomers and biological tissues possess the remarkable ability to sustain large deformation, and typically exhibit a complex, nonlinear, mechanical response [1,2]. Modelling and predicting the behaviour of such rubber-like solids is relevant for a wide range of applications such as biomechanics [3,4], soft robotics [5,6]

© 2026 The Authors. Published by the Royal Society under the terms of the Creative Commons Attribution License http://creativecommons.org/licenses/by/4.0/, which permits unrestricted use, provided the original author and source are credited.

THE ROYAL SOCIETY PUBLISHING

Downloaded from royalsocietypublishing.org/rspa/article-pdf/doi/10.1098/rspa.2026.0254/6169189/rspa.2026.0254.pdf
by guest
on 05 November 2026

and the design of bio-inspired materials [7,8]. Yet, finding a universal material constitutive law that can accurately describe the mechanical behaviour of a given elastomer for all possible deformation fields and for the whole range of achievable extensions remains an outstanding challenge [9].

Recalling the origins of rubber elasticity helps in navigating the large number of constitutive models proposed in the literature. Rubber-like solids are composed of long-chain molecules that interact through weak forces and that are linked together to form a sparse network whose mechanical properties are of entropic nature [2]. Using idealized chain models, it is possible to obtain the chain's spatial conformation and to determine the macroscopic network properties through a statistical averaging procedure. Assuming the chains never approach their extended length, i.e. using the Gaussian chain approximation, this micro-mechanical approach yields the neo-Hookean strain energy density [2].

Further developments addressed the limitations of the neo-Hookean theory evidenced by static experiments across multiple deformation classes [10]. They followed two distinct paths: (i) The statistical theory was refined by relaxing the assumptions of the Gaussian chain model, enabling the capture of the strain-stiffening effect at large elongation associated with finite chain extensibility [11,12]. (ii) Phenomenological continuum mechanics models were introduced to account for the experimental deviations from neo-Hookean predictions. Most notably, Mooney and Rivlin proposed to augment the neo-Hookean constitutive law with an additional term, the so-called C_2 term [13,14], and Ogden suggested an empirical form of the strain energy that allowed, for the first time, to fit a single model across a variety of deformation classes and a large range of strain [15]. Rather than being mutually exclusive, these two approaches have proven to be complementary. Non-Gaussian models have been connected to generalized neo-Hookean continuum models that capture strain hardening [16]. For example, Horgan & Saccomandi [17] evidenced the link between the Arruda–Boyce model [12] and the phenomenological Gent model [18]. The additional term proposed by Mooney and Rivlin can also be linked to micro-mechanical considerations by modelling the constraints from neighbouring chains using a tube model [16,19], yielding a C_2 contribution of the form proposed by Gent & Thomas [20].

Assessing the performance of the constitutive laws introduced to overcome the limitations of the neo-Hookean strain energy requires determining their ability to fit experimental data for all deformation classes and all extensions. However, Ogden *et al.* [21] identified that the fitting procedure faces a fundamental challenge: multiple sets of parameters can give an equally good fit of uniaxial extension data, but markedly different predictions for other deformations or for simple boundary value problems. Destrade *et al.* [9] took a key step towards the resolution of this issue by delineating a methodical procedure to find a unique optimal parameter set when fitting simple extension data, the most commonly performed test to characterize rubber-like solids. They evidenced that any standard linear combination of a generalized neo-Hookean model and a C_2 term captures the mechanical response in simple tension, highlighting the need to perform experiments across multiple deformation classes to discriminate constitutive models.

Our aim here is to show that dynamic measurements provide an alternative approach. We demonstrate how guided waves propagating in an elastomer plate undergoing uniaxial extension reveal model sensitivities that remain hidden in the corresponding static test. We first describe the experiments from which we obtain the dispersion relations of the two lowest-order in-plane modes and the lowest-order out-of-plane mode propagating parallel and perpendicular to the direction of elongation (§2). In §3, we recall the modelling of the mechanical response of nearly incompressible hyperelastic materials within the nonlinear elasticity framework. We then detail how we predict the dispersion relation of waves propagating in our samples, which, unlike for static tests, requires coupling hyperelasticity and viscoelasticity within the acoustoelastic theory framework. We focus on how guiding, viscoelasticity and prestress affect wave dispersion and explain how we compare the experimental dispersion relations to predictions that depend on the parameters extracted from fitting the uniaxial stress–strain curve using the procedure of Destrade *et al.* [9]. We also highlight how guided modes carry additional insight into the constitutive law. In §4, we present the results of this comparison, distinguishing the three regimes introduced

Downloaded from royalsocietypublishing.org/rspa/article-pdf/doi/10.1098/rspa.2026.0254/6169189/rspa.2026.0254.pdf
by guest
on 05 November 2026

in [9]: the small to moderate elongation regime, the strain-hardening regime and the large deformation regime. We show that while multiple constitutive models yield indistinguishable fits of the uniaxial stress–strain curve, their predictions for wave dispersion diverge significantly. We evidence that the dynamic measurements are sensitive to the form of the C_2 energy term, unlike the static response, but that any standard generalized neo-Hookean model captures the guided waves behaviour in the limiting chain regime. Finally, we conclude by contrasting our observations with those gained by considering other deformation classes and discuss the perspectives of this work in §5.

2. Measuring guided elastic waves in a plate

We characterize wave propagation in a plate subjected to a large, static, uniaxial deformation where we impose the principal stretch λ in the direction $\boldsymbol{e}_1$, as sketched in figure 1*a*. In the experimentally accessible frequency range, only the three zero-order guided modes propagate in the plate: (i) the non-dispersive shear horizontal mode SH_0, which corresponds to shear waves polarized in the $(\boldsymbol{e}_1, \boldsymbol{e}_3)$ plane, and the two Lamb modes; (ii) the S_0 mode, which resembles a longitudinally polarized mode in the plane $(\boldsymbol{e}_1, \boldsymbol{e}_3)$; and (iii) the flexural A_0 mode, which mostly exhibits out-of-plane displacement in the direction $\boldsymbol{e}_2$ [22]. We extend the experiments of Delory *et al.* [23] that obtained the dispersion relations of the in-plane SH_0 and S_0 modes, propagating both parallel and perpendicular to the elongation direction for varying values of λ, by additionally measuring the dispersion curves of the out-of-plane A_0 mode.

(a) In-plane modes

We recall the experimental set-up and procedure used to obtain the dispersion relation of in-plane modes by Delory *et al.* [23]. A square plate made of a soft elastomer, Ecoflex OO-30, with size $L_0 = 60\,\text{cm}$ and thickness $h_0 = 3\,\text{mm}$ is held vertically using clamps at its top and bottom edges (figure 1*a*). By setting the distance between the clamps $L = \lambda L_0$, we impose a nearly uniaxial deformation described by the principal stretches $(\lambda_1 = \lambda, \lambda_2, \lambda_3)$. Tracking the position of four markers placed at the centre of the plate allows us to measure the in-plane stretch ratios. We find that the imposed deformation is not exactly uniaxial, $\lambda_3 = \lambda^{-0.41}$, as the clamps prevent stretching in the $\boldsymbol{e}_3$ direction. We also emphasize that the vertical plate is not in its reference configuration in the absence of an imposed elongation. Its own weight generates a small non-homogeneous deformation, corresponding to $\lambda = 1.03$ at the centre of the plate, which affected the measured values of λ in the work of Delory *et al.* in [23]. Here, we multiply all values of λ reported in [23] by 1.03 to correct for this initial elongation, but neglect the non-homogeneous nature of the deformation induced by gravity. A line source driven by a shaker excites monochromatic elastic waves with frequencies f ranging from 50 to 300 Hz in the directions $\boldsymbol{e}_1$, parallel to the direction of elongation, or $\boldsymbol{e}_3$, perpendicular to the direction of elongation for values of λ spanning the range from 1.03 to 2.27. The in-plane displacement (u_1, u_3) associated with the propagation of the small-amplitude waves is recorded using stroboscopic imaging in combination with a digital image correlation algorithm [24]. For additional details on the experimental procedure to measure the in-plane guided modes, we refer the reader to [23,24].

Performing spatial Fourier transforms on each measured monochromatic displacement field enables us to obtain the dispersion relations of waves propagating in the parallel and perpendicular directions for $\lambda \in [1.03, 2.27]$ (figure 1*b*,*c*). We indeed observe that two modes propagate and identify the SH_0 and S_0 modes from their expected velocity in the long-wavelength limit in the absence of pre-stress, V_T and $V_P = 2V_T$, respectively, where V_T is the shear wave velocity [22,25]. As λ increases, wave propagation becomes anisotropic: parallel to the imposed stretch, both phase velocities increase with λ, similarly to a string in the tension regime, while in the perpendicular direction, the velocities of the SH_0 and S_0 modes are barely affected.

Downloaded from royalsocietypublishing.org/rspa/article-pdf/doi/10.1098/rspa.2026.0254/6169189/rspa.2026.0254.pdf
by guest
on 05 November 2026

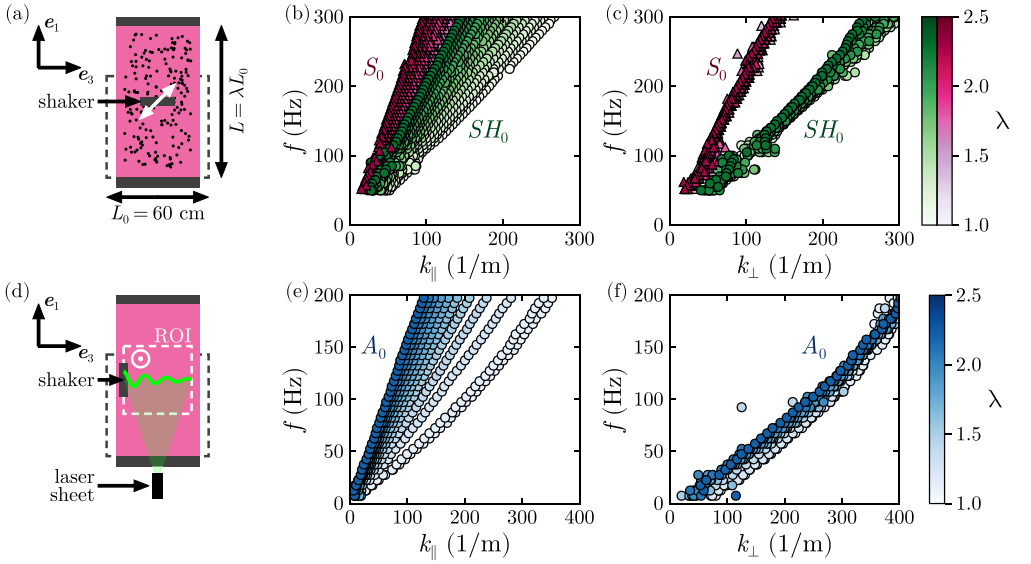


Figure 1. (a) Sketch of the experimental set-up used to measure the dispersion curves of the in-plane modes in a soft elastomer plate. The white arrows indicate the direction of shaker motion, which enables the simultaneous generation of the SH_0 and S_0 modes. (b-c) Dispersion relations of the in-plane SH_0 (green circles) and S_0 (pink triangles) modes propagating parallel and perpendicular to the direction of elongation for $\lambda \in [1.03, 2.27]$. (d) Schematic of the experimental set-up used to obtain the dispersion relation of the out-of-plane A_0 mode. The shaker motion is in the $\boldsymbol{e}_2$ direction as indicated by the white symbol. (e-f) Dispersion curves of the A_0 mode propagating parallel and perpendicular to the imposed stretch for $\lambda \in [1.11, 2.22]$.

(b) Out-of-plane mode

We use a similar set-up to measure the dispersion curves of the flexural mode (figure 1*d*). We prepare an Ecoflex OO-30 plate with dimensions $L_0 = 60$ cm and $h_0 = 2.5$ mm and follow the same procedure to impose an almost uniaxial homogeneous deformation. Similarly, we track markers to measure the in-plane principal stretches and obtain $\lambda_3 = \lambda^{-0.39}$. After the static uniaxial deformation is imposed, a shaker drives a line source in the $\boldsymbol{e}_2$ direction, creating small-amplitude out-of-plane waves. The source generates a quadratic chirp signal with instantaneous frequency varying from 200 to 1 Hz in 0.7 s. We record the deflection of a laser sheet projected in oblique incidence and passing through the plate's centre and oriented along the $\boldsymbol{e}_1$ or $\boldsymbol{e}_3$ direction with a charged-coupled device camera working at an acquisition frequency of 1 kHz. The out-of-plane displacement $u_2(x_i, t)$, with $i = 1, 3$, is directly proportional to the in-plane deflection of the laser line, which we extract from the images. We restrict the measurement region of interest (ROI) to a 23.5 cm × 23.5 cm square, positioned at the centre of the plate in each deformed configuration, where the influence of the clamped boundary conditions at the top and bottom edges of the plate vanishes and the deformation is homogeneous [23].

We then obtain the dispersion curves of out-of-plane waves propagating in directions 1 and 3 by performing the two-dimensional Fourier transform of $u_2(x_i, t)$ and by extracting maxima in the (k_{x_i}, f) space. In figure 1*e-f*, we represent the dispersion relations of the A_0 mode parallel and perpendicular to the direction of elongation for values of the static stretch λ ranging from 1.11 to 2.22. Even for the lowest imposed stretch, we observe that wave propagation is anisotropic. Indeed, the A_0 mode is very sensitive to the imposed elongation. It quickly loses its expected parabolic shape in the long-wavelength regime to become non-dispersive in the direction of elongation for the largest imposed values of λ. Perpendicular to the direction of propagation, the dispersion curves are less dramatically affected by the imposed stretch, yet they are more markedly influenced than for the two in-plane modes.

Downloaded from royalsocietypublishing.org/rspa/article-pdf/doi/10.1098/rspa.2026.0254/6169189/rspa.2026.0254.pdf
by guest
on 05 November 2026

Having evidenced how a large uniaxial deformation affects the propagation of the three zero-order modes propagating in a plate, both parallel and perpendicular to the direction of imposed stretch, we turn to the modelling of nearly incompressible hyperelastic materials.

3. Material modelling

(a) Nonlinear elasticity for hyperelastic materials

We are interested in nearly incompressible isotropic hyperelastic materials whose mechanical behaviour is described by a strain energy density W. The constitutive law is a function of the first three principal invariants of the left Cauchy–Green tensor $\boldsymbol{B} = \boldsymbol{F} \cdot \boldsymbol{F}^T$:

$$I_1 = \mathrm{tr}(\boldsymbol{B}) = \lambda_1^2 + \lambda_2^2 + \lambda_3^2,$$
$$I_2 = \frac{1}{2}\left(\mathrm{tr}(\boldsymbol{B})^2 - \mathrm{tr}(\boldsymbol{B}^2)\right) = \lambda_2^2\lambda_3^2 + \lambda_1^2\lambda_3^2 + \lambda_1^2\lambda_2^2,$$
$$I_3 = \det(\boldsymbol{B}) = \lambda_1^2\lambda_2^2\lambda_3^2 = J^2,$$

where $\boldsymbol{F}$ is the deformation gradient and λ_i are the principal stretches of the deformation.

The strain energy density must also satisfy the following additional constraints [26]: (i) For normalization, we impose that W vanishes in the reference configuration. (ii) To reflect that a sample cannot be indefinitely expanded or compressed, W should become infinite as J tends to $+\infty$ and 0^+, respectively. (iii) We assume that the Cauchy stress vanishes in the reference configuration. (iv) W must be compatible with the linear elasticity theory so that

$$\mu_0 = 2\left[\frac{\partial W}{\partial I_1} + \frac{\partial W}{\partial I_2}\right]_{(I_1=3,I_2=3,I_3=1)}, \tag{3.1}$$

$$\frac{\kappa_0}{4} + \frac{\mu_0}{3} = \left[\frac{\partial^2 W}{\partial I_1^2} + 4\frac{\partial^2 W}{\partial I_1 \partial I_2} + 4\frac{\partial^2 W}{\partial I_2^2} + 2\frac{\partial^2 W}{\partial I_1 \partial I_3} + 4\frac{\partial^2 W}{\partial I_2 \partial I_3} + \frac{\partial^2 W}{\partial I_3^2}\right]_{(3,3,1)}, \tag{3.2}$$

where μ_0 and κ_0 are the infinitesimal shear and bulk modulus, respectively. More generally, we use strain energy densities compatible with fourth-order weakly nonlinear elasticity, which has been shown to be the minimal model to capture fully nonlinear effects [9,27].

We build compressible strain energy density functions by adding a volumetric term to the classical incompressible strain energy density W_I. We decompose the deformation into an isochoric and a volumetric part, so that W can be written as

$$W\left(\bar{I}_1, \bar{I}_2, J\right) = W_{dev}\left(\bar{I}_1, \bar{I}_2\right) + W_{vol}\left(J\right), \tag{3.3}$$

where $\bar{I}_1 = I_1/J^{2/3}$, $\bar{I}_2 = I_2/J^{4/3}$ and W_{vol} is the volumetric contribution. Indeed, this expression must satisfy the condition that $W_{dev} = W_I$ in the isochoric case when $J^2 = 1$ [26]. In the following, we fix the form of the volumetric contribution:

$$W_{vol} = \frac{\kappa_0}{2}(J-1)^2. \tag{3.4}$$

The nearly incompressible nature of the materials under consideration is encoded in the ratio μ_0/κ_0, which is a small, but non-zero parameter.

Finally, for such materials, the Cauchy stress is related to the strain energy function by

$$\boldsymbol{\sigma} = \frac{1}{J}\frac{\partial W}{\partial \boldsymbol{F}} \cdot \boldsymbol{F}^T. \tag{3.5}$$

Downloaded from royalsocietypublishing.org/rspa/article-pdf/doi/10.1098/rspa.2026.0254/6169189/rspa.2026.0254.pdf
by guest
on 05 November 2026

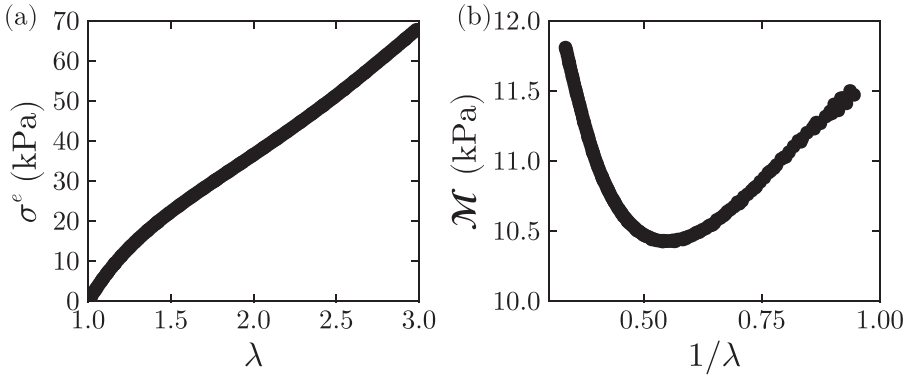


Figure 2. Uniaxial extension test of an Ecoflex 00-30 sample. (a) Engineering stress σ^e as a function of the stretch ratio in the direction of elongation, λ. (b) Same data as in (a) represented in the Mooney space (equation (3.7)).

(b) Fitting the strain energy density to uniaxial data

We recall the interpretation of the data gathered during a traction test and the fitting procedure detailed in Destrade *et al.* [9]. In such a test, a uniaxial elongation, corresponding to $\lambda_1 = \lambda$, is imposed and the force exerted on the sample in the direction of elongation is recorded. By assuming that the deformation is homogeneous and that the material is incompressible, we obtain the principal stretches as $(\lambda, 1/\sqrt{\lambda}, 1/\sqrt{\lambda})$ and use the incompressible form of W. In figure 2*a*, we display the data gathered while performing such a test on an Ecoflex 00-30 sample. We represent the engineering stress in the direction of elongation σ^e, that is, the force divided by the cross-sectional area of the sample in the reference configuration, as a function of λ. In this idealized testing configuration, it is straightforward to compute σ^e from the strain energy density:

$$\sigma^e = \frac{\partial W_I}{\partial \lambda} = 2\left(\lambda - \frac{1}{\lambda^2}\right)\left(\frac{\partial W_I}{\partial I_1} + \frac{1}{\lambda}\frac{\partial W_I}{\partial I_2}\right). \tag{3.6}$$

At this point, it is convenient to introduce the Mooney transform

$$\mathcal{M}(\xi) = \frac{\partial W_I}{\partial I_1} + \xi \frac{\partial W_I}{\partial I_2}, \quad \text{where} \quad \mathcal{M} = \frac{\sigma^e}{2(\lambda - 1/\lambda^2)} \quad \text{and} \quad \xi = \frac{1}{\lambda}. \tag{3.7}$$

We represent $\mathcal{M}$ as a function of $1/\lambda$, the so-called Mooney plot (figure 2*b*) and observe that the Mooney transform emphasizes the range of stretch $\lambda \in [1, 2]$. The Mooney plot crucially allows one to distinguish three successive stretch regimes: the small to moderate strain regime, where $\mathcal{M}$ decreases as λ increases (here typically for ξ from 1 down to 0.6), the strain-hardening regime corresponding to the upturn in the Mooney plot (for ξ in between 0.6 and 0.4), and the large deformation regime in which the stress rises dramatically at low values of $1/\lambda$ [9]. We also emphasize that the initial decrease in the Mooney plot already evidences the limitations of the neo-Hookean model,

$$W_I(I_1) = \frac{\mu_0}{2}(I_1 - 3), \tag{3.8}$$

which predicts a constant value $\mathcal{M} = \mu_0/2$ (equation (3.7)) and thus must be complemented by an additional C_2 term, dependent on I_2, even at small elongations [9].

We now focus on matching the traction test data to mathematical models of W_I. We look for the set of parameters $\boldsymbol{p}$, involved in the definition of W_I, that best fits the m experimental data points obtained during the traction test. To find this set of parameters, we follow Destrade *et al.* [9] and

Downloaded from royalsocietypublishing.org/rspa/article-pdf/doi/10.1098/rspa.2026.0254/6169189/rspa.2026.0254.pdf
by guest
on 05 November 2026

choose to minimize the 2-norm of the relative residuals $r_i(\boldsymbol{p})$ in the Mooney space,

$$\|\boldsymbol{r}(\boldsymbol{p})\|_2{}^2 = \sum_{i=1}^{m} r_i(\boldsymbol{p})^2 = \sum_{i=1}^{m} \left(\frac{\mathcal{M}(\lambda_i, \boldsymbol{p})}{\mathcal{M}_i} - 1 \right)^2, \tag{3.9}$$

either using a least-squares approach, or, when the problem is nonlinear with respect to $\boldsymbol{p}$, using a genetic algorithm to ensure we obtain a global minimum [28]. We note that this approach has the advantage of ensuring that the fit parameters are the same regardless of the stress; that is, we could have equivalently minimized the norms of the relative residuals in the engineering or Cauchy space.

(c) Guided waves dispersion relations

We describe how to compute the dispersion relation of small-amplitude guided waves propagating in a plate subjected to a large homogeneous deformation from the fitted form of the strain energy density. These predictions are obtained from the acoustoelastic theory, which describes incremental motions superimposed on the large static deformation [29,30]. Within this framework, the incremental displacement $\boldsymbol{u}$ obeys a wave-like equation,

$$C^0_{jikl}\left(\lambda_1, \lambda_2, \lambda_3, \boldsymbol{p}\right) \frac{\partial^2 u_k}{\partial x_j \partial x_l} = \rho \frac{\partial^2 u_i}{\partial t^2}, \tag{3.10}$$

where the fourth-order elasticity tensor has been replaced by its push-forward version in the deformed configuration $\boldsymbol{C}^0\left(\lambda_1, \lambda_2, \lambda_3, \boldsymbol{p}\right)$ [29,30].

An additional difficulty arises for soft elastomers such as those used in our experiments: describing wave propagation requires taking into account their viscoelastic behaviour [23,31,32]. According to independent rheological measurements [33], we model the frequency-dependent properties of Ecoflex OO-30 using the fractional derivative Kelvin–Voigt model,

$$\mu = \mu_0 \left(1 + (\mathrm{i}\omega\tau)^n\right), \tag{3.11}$$

where μ_0 is the infinitesimal shear modulus and τ, n are material parameters [34,35]. The viscoelastic parameters are obtained by minimizing the relative error between the fractional Kelvin–Voigt model and the real (μ') and imaginary (μ'') parts of the shear modulus measured using a rheometer in plate–plate configuration (figure 3*a*). We find $\mu_0 = 25.3\,\mathrm{kPa}$, $\tau = 249\,\mu\mathrm{s}$ and $n = 0.3$. We keep the values of τ and n constant for the remainder of the paper, but we choose to determine μ_0 from the uniaxial extension test, which has the advantage of being conducted on a sample prepared in the same conditions as that used in the experiments. We combine viscoelasticity and hyperelasticity by decomposing the Cauchy stress tensor into a hyperelastic part, given by equation (3.5), and a dynamic part, following the work of Destrade *et al.* [36]. Considering only the first-order term coupling viscoelasticity and hyperelasticity as proposed by Delory *et al.* [23], we obtain the following approximation of the dynamic stress:

$$\boldsymbol{\sigma}_d = 2\eta \boldsymbol{D} + \beta \left(\boldsymbol{D} \cdot \boldsymbol{B} + \boldsymbol{B} \cdot \boldsymbol{D}\right), \tag{3.12}$$

with

$$\boldsymbol{D} = \boldsymbol{F} \cdot \frac{\partial^n}{\partial t^n} \left(\frac{1}{2} \left(\boldsymbol{I} - \boldsymbol{C}^{-1} \right) \right) \cdot \boldsymbol{F}^T,$$

where η is the dynamic viscosity, β is a parameter coupling the elastic and viscous responses and $\boldsymbol{C} = \boldsymbol{F}^T\boldsymbol{F}$ is the right Cauchy–Green tensor [23,36,37]. Here, $\boldsymbol{D}$ is a material frame-independent analogue of the Eulerian strain rate tensor $\boldsymbol{D} = 1/2\left(\boldsymbol{L} + \boldsymbol{L}^T\right)$, where $\boldsymbol{L} = \dot{\boldsymbol{F}}\boldsymbol{F}^{-1}$ is the velocity gradient, to which it reduces in the viscous case ($n = 1$), allowing us to recover the usual Newtonian

Downloaded from royalsocietypublishing.org/rspa/article-pdf/doi/10.1098/rspa.2026.0254/6169189/rspa.2026.0254.pdf
by guest
on 05 November 2026

shear viscosity term. Other choices for the form of $\boldsymbol{D}$ are possible, and we refer the reader to Berjamin & Destrade [37] for a detailed discussion. We stress that the inclusion of the fractional time derivative enables us to match the frequency-dependent properties of Ecoflex OO-30 described by equation (3.11). By computing the incremental stress, taking into account the dynamic contribution, we obtain a frequency-dependent modified elasticity tensor $\boldsymbol{C}^0$, which now reads

$$C^0_{jikl}(\lambda_1, \lambda_2, \lambda_3, \boldsymbol{p}, \omega, \beta') = C^0_{jikl}(\lambda_1, \lambda_2, \lambda_3, \boldsymbol{p}) + \mu_0 I_{jikl}\left(1 + \beta' \frac{\lambda_i^2 + \lambda_j^2 - 2}{2}\right)(\mathrm{i}\omega\tau)^n, \tag{3.13}$$

with $I_{jikl} = (\delta_{jk}\delta_{il} + \delta_{jl}\delta_{ik})$, and β' is a parameter coupling hyperelasticity and viscoelasticity [23,37]. We compute the push-forward of the elasticity tensor for a given choice of mathematical model for the strain energy W using the definitions of its coefficients given in [38], which are identical to those given in [29,30] with a permutation of the last two indices. We note that taking into account the coupling between viscoelasticity and hyperelasticity results in the introduction of an extra adjustable parameter β', whose value must be determined from dynamic measurements.

We then proceed to determine the dispersion relation of guided elastic waves propagating in the plate parallel and perpendicular to the direction of imposed elongation $\lambda_1 = \lambda$, with a focus on the shear horizontal, pseudo-longitudinal and flexural fundamental modes probed in our experiments. In this situation, we experimentally access only the in-plane principal stretches λ and λ_3. We thus further take the nearly incompressible limit, $J \to 1$, which, in combination with the boundary condition $\sigma_2 = 0$, allows us to eliminate the λ_2 dependence and to get expressions for the coefficients of the tensor $\boldsymbol{C}^0\left(\lambda, \lambda_3, \boldsymbol{p}, \omega, \beta'\right)$ [38,39]. Guided waves are propagative solutions of equation (3.10) that satisfy the boundary conditions,

$$\boldsymbol{e}_2 \cdot \boldsymbol{\sigma}\big|_{\pm h/2} = 0, \tag{3.14}$$

where $h = h_0\lambda_2 = h_0\lambda^{-1}\lambda_3^{-1}$. For shear horizontal modes, reflections at the boundaries do not involve coupling between different polarizations and the phase velocity of the SH_0 mode is directly given by the bulk shear wave velocity. It reads in the directions parallel and perpendicular to the elongation

$$\rho V^2_{SH_0,\parallel} = C^0_{1331}, \tag{3.15a}$$

$$\rho V^2_{SH_0,\perp} = C^0_{3113}. \tag{3.15b}$$

Note that in the absence of prestress these two quantities are equal owing to the symmetries of the elasticity tensor, a fact that is implicitly assumed when adopting the Voigt notation.

For the pseudo-longitudinal S_0 and the flexural A_0 Lamb modes, the coupling between shear vertical and longitudinal polarizations at the boundaries complexifies the obtention of the spectrum. Nevertheless, Rogerson & Prikazchikova [40] derived long-wavelength approximations for the phase velocities of the S_0 modes:

$$\rho V^2_{S_0,\parallel} = C^0_{1111} - \frac{{C^0_{1122}}^2}{C^0_{2222}}, \tag{3.16a}$$

$$\rho V^2_{S_0,\perp} = C^0_{3333} - \frac{{C^0_{3322}}^2}{C^0_{2222}} \tag{3.16b}$$

and the A_0 modes

$$\rho V^2_{A_0,\parallel} = C^0_{1221} - C^0_{2112}, \tag{3.17a}$$

$$\rho V^2_{A_0,\perp} = C^0_{3223} - C^0_{2332}. \tag{3.17b}$$

Again, in the absence of initial deformation, the symmetries of the elasticity tensor yield a null velocity for the A_0 mode, which corresponds to the well-known parabolic nature of its dispersion relation.

Downloaded from royalsocietypublishing.org/rspa/article-pdf/doi/10.1098/rspa.2026.0254/6169189/rspa.2026.0254.pdf
by guest
on 05 November 2026

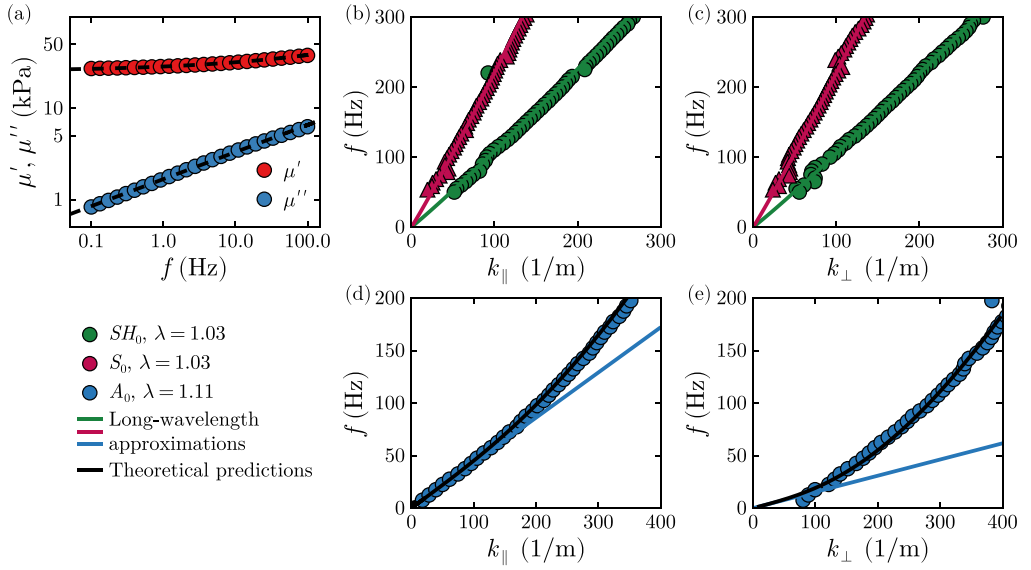


Figure 3. (a) Rheological measurement of the complex shear modulus of Ecoflex 00-30. We plot the real and imaginary parts of the shear modulus μ' and μ'', respectively. The dashed lines show the fit of the fractional Kelvin–Voigt model to the data. (b-c) Dispersion relations of the in-plane SH_0 and S_0 modes propagating parallel or perpendicular to the direction of elongation for $\lambda = 1.03$. The solid lines represent the long-wavelength approximations defined in equations (3.15) and (3.16). (d-e) Dispersion relations of the out-of-plane A_0 mode propagating parallel or perpendicular to the direction of elongation for $\lambda = 1.11$. The blue lines stand for the long-wavelength predictions of equation (3.17), and the black lines show the full semi-analytical predictions.

Anticipating later discussions, we evidence the relationship between the phase velocities in the long-wavelength limit and the strain energy density using the formulas given in [38]. For the SH_0 mode, we find

$$\rho V^2_{SH_0,\parallel} = \frac{\lambda^2}{\lambda^2 - \lambda_3^2}\frac{1}{J}\left(\lambda\frac{\partial W}{\partial \lambda} - \lambda_3\frac{\partial W}{\partial \lambda_3}\right) + \mu_0\left(1 + \beta'\frac{\lambda^2 + \lambda_3^2 - 2}{2}\right)(\mathrm{i}\omega\tau)^n, \tag{3.18a}$$

$$\rho V^2_{SH_0,\perp} = \frac{\lambda_3^2}{\lambda^2 - \lambda_3^2}\frac{1}{J}\left(\lambda\frac{\partial W}{\partial \lambda} - \lambda_3\frac{\partial W}{\partial \lambda_3}\right) + \mu_0\left(1 + \beta'\frac{\lambda^2 + \lambda_3^2 - 2}{2}\right)(\mathrm{i}\omega\tau)^n. \tag{3.18b}$$

We highlight that by subtracting these two velocities, we can recover the state of stress in the plate $\sigma_1 - \sigma_3$ using $\sigma_1 = J^{-1}\lambda\partial W/\partial\lambda$ and $\sigma_3 = J^{-1}\lambda_3\partial W/\partial\lambda_3$, independent of the material rheology, as noted in [41,42]. Similarly, we obtain the velocity of the A_0 mode parallel and perpendicular to the direction of propagation. Both phase speeds are independent of the material rheology and thus of β' and are related to the stress in the plate by

$$\rho V^2_{A_0,\parallel} = \sigma_1, \tag{3.19a}$$

$$\rho V^2_{A_0,\perp} = \sigma_3, \tag{3.19b}$$

where we took into account the boundary condition $\sigma_2 = 0$, and considered that the deformation is not exactly uniaxial, that is, $\lambda_3 \neq \lambda^{-1/2}$, as observed in our experiments. Linking the phase velocity of the S_0 mode to W does not yield an expression that can be easily interpreted. However, we emphasize that the velocity depends on second-order derivatives of W with respect to λ_i, that is, to the derivative of stress with stretch, unlike for the SH_0 and A_0 modes where the velocities are only related to the stress in the plate.

Downloaded from royalsocietypublishing.org/rspa/article-pdf/doi/10.1098/rspa.2026.0254/6169189/rspa.2026.0254.pdf
by guest
on 05 November 2026

We discuss the relevance of the above approximations by comparing their predictions with the dispersion relations of the three fundamental modes in the parallel and perpendicular directions for $\lambda = 1.03$ for the in-plane modes, and $\lambda = 1.11$ for the out-of-plane mode (figure 3*b–e*). Here, our goal is not to discriminate between different mathematical models for W, and we compute the modified elasticity tensor for the Mooney–Rivlin strain energy density [13,14], which was found to accurately describe their data by Delory *et al.* [23]. As the measurements of the in-plane and out-of-plane modes were conducted on distinct Ecoflex OO-30 samples, we use two sets of parameters $\boldsymbol{p}$, which we extract by fitting the Mooney–Rivlin strain energy density to the uniaxial extension data presented in figure 2 for the out-of-plane case, and in fig. 6 of [23] for the in-plane case. We use the procedure described in §3 that we systematically detail in §4. We find that the two sets of parameters are equivalent once normalized by the value of the infinitesimal shear modulus $\mu_0 = 31.1$ kPa, and $\mu_0 = 23.4$ kPa for the in-plane and out-of-plane case, respectively. The principal stretches $\lambda_1 = \lambda$ and λ_3 are measured and we, for now, take the value of the remaining parameter, $\beta' = 0.29$, from the work of Delory *et al.* [23]. For both in-plane modes, the long-wavelength approximation (solid lines in figure 3*b,c*) accurately captures the dispersion relation in the whole experimental range. By contrast, for the flexural mode (figure 3*d,e*), the approximations are satisfying only for a limited wavenumber range, especially perpendicular to the direction of elongation, as expected for this bending mode, which displays a parabolic dispersion relation in the reference configuration.

The inability of equations (3.17) to fully capture the dispersion relation of the flexural mode highlights the need to go beyond long-wavelength predictions. We do so by searching for non-trivial solutions to the system of equations (3.10) and (3.14) using a semi-analytical method. After inserting the displacement ansatz $\boldsymbol{u} = \boldsymbol{u}\left(k_i, x_2, \omega\right) e^{\mathrm{i}(k_i x_i - \omega t)}$ with $i = 1, 3$, we discretize the problem in the x_2 direction using the spectral collocation method [43,44]. We obtain the dispersion relation as pairs (k_i, ω) that are solution to an algebraic eigenvalue problem where the wavenumber is complex valued, a key to successfully modelling viscoelastic media [45]. Our implementation, adapted from [39,46], is detailed and available in [47]. The semi-analytical predictions for the dispersion relation of the A_0 mode are shown with a black line in figure 3*d,e* and exhibit excellent agreement with the experimental measurements.

We now possess all the necessary tools to fit the strain energy density to uniaxial extension data and to predict the dispersion relations of guided modes propagating in a homogeneously deformed plate characterized by the strain energy W, enabling us to perform a comparison with our dynamic measurements. We highlight that our experiments have the potential to provide new pieces of information over a static test: the pseudo-longitudinal mode is sensitive to the derivative of stress with strain, and the flexural mode gives insight on the stress perpendicular to the direction of elongation. However, these additional data come at the expense of involving an extra parameter β' that accounts for the coupling between hyperelasticity and viscoelasticity.

4. Results

We now compare our experimental measurements to predictions obtained for different constitutive laws fitted on the uniaxial extension data of figure 2. We successively address the three stretch regimes evidenced in the Mooney plot to eventually describe the material behaviour over the whole range of imposed elongation.

(a) Small to moderate strain regime

We first focus on the small to moderate strain regime, which corresponds to the linear decrease in the Mooney plot (figure 4*a*), where the neo-Hookean model must be augmented by the addition of a C_2 term dependent on the second invariant I_2. We consider three models that can in principle capture the decrease in the Mooney plot and differ only by the functional form of the I_2 term:

Downloaded from royalsocietypublishing.org/rspa/article-pdf/doi/10.1098/rspa.2026.0254/6169189/rspa.2026.0254.pdf
by guest
on 05 November 2026

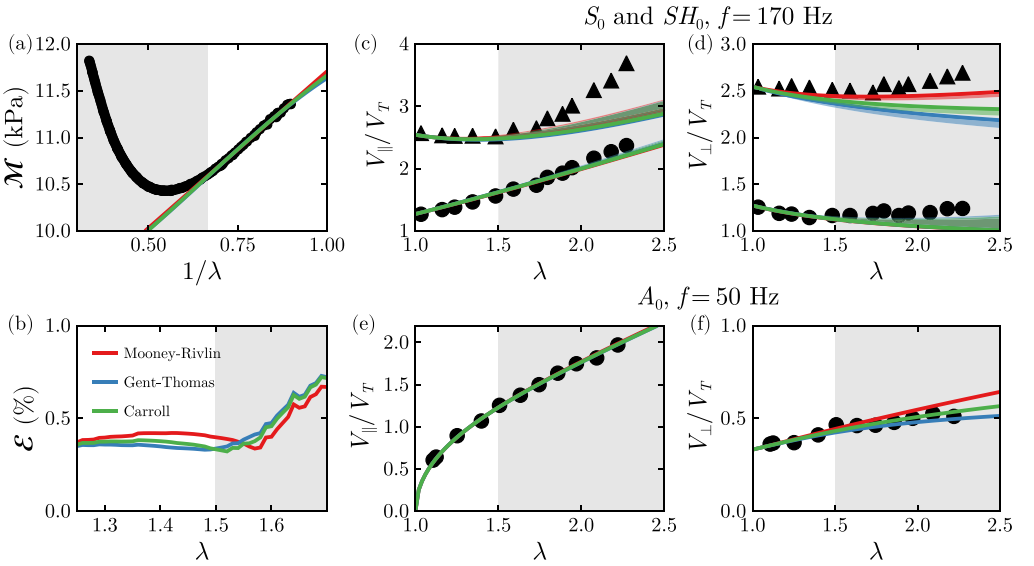


Figure 4. (a) Mooney plot for Ecoflex 00-30 showing the fits of the Mooney–Rivlin, Gent–Thomas and Carroll models in the small to moderate stretch regime (solid lines). The greyed-out region evidences the points for which $\lambda > 1.5$ that are excluded from the fitting procedure. (b) Maximum relative error $\mathcal{E}$ as a function of the fit endpoint for the three models considered in (a). (c-d) Normalized wave velocities for the SH_0 (dots) and S_0 (triangles) modes propagating parallel and perpendicular to the direction of elongation as a function of λ for $f = 170$ Hz. The solid lines are long-wavelength predictions computed from equations (3.15) and (3.16). The shaded area around the prediction lines corresponds to 95% confidence intervals, resulting from the uncertainty on the value of β'. (e-f) Normalized wave velocities in the directions $\boldsymbol{e}_1$ and $\boldsymbol{e}_3$ for the A_0 mode for $f = 50$ Hz. Parallel to the direction of propagation, the predictions come from the approximation equation (3.17*a*) while perpendicular to the direction of propagation we represent the results of the semi-analytical theory.

— the Mooney–Rivlin model [13]

$$W_I(I_1, I_2) = \frac{C_1}{2}(I_1 - 3) + \frac{C_2}{2}(I_2 - 3), \tag{4.1}$$

— the Gent–Thomas model [20]

$$W_I(I_1, I_2) = \frac{C_1}{2}(I_1 - 3) + \frac{3C_2}{2}\ln\left(\frac{I_2}{3}\right), \tag{4.2}$$

— the Carroll model [48]

$$W_I(I_1, I_2) = \frac{C_1}{2}(I_1 - 3) + \sqrt{3}C_2\left(\sqrt{I_2} - \sqrt{3}\right). \tag{4.3}$$

We fit these two-parameter models to the uniaxial data of figure 4*a* using the goodness of fit metric defined in equation (3.9) by introducing generalized Mooney transforms [49]. Similarly, as equation (3.7) enables the Mooney–Rivlin model to be represented as a line in the $(\mathcal{M}, \xi)$ space, these transforms allow us to fit the Gent–Thomas and Carroll models using linear regressions. However, it requires one to rigorously determine the extent of the small to moderate stretch regime, which we do by recording the maximum of the relative error,

$$\mathcal{E} = \max_i \left| r_i(\boldsymbol{p}^*) \right|, \tag{4.4}$$

while varying the fit endpoint, as proposed by Destrade *et al.* [9]. We display the results in figure 4*b*. The maximum relative error rises sharply when the fitted endpoint corresponds to a

Downloaded from royalsocietypublishing.org/rspa/article-pdf/doi/10.1098/rspa.2026.0254/6169189/rspa.2026.0254.pdf
by guest
on 05 November 2026

Table 1. Material parameters C_1 and C_2 for the Mooney–Rivlin, Gent–Thomas and Carroll hyperelastic models obtained by fitting the uniaxial extension data for $\lambda < 1.5$. We quantify the goodness of fit by recording the maximal relative error $\mathcal{E}$. We also list the values of the shear modulus $\mu_0 = C_1 + C_2$ and of the parameter coupling hyperelasticity and viscoelasticity β'.

model	C_1 (kPa)	C_2 (kPa)	$\mathcal{E}$ (%)	μ_0 (kPa)	β'
Mooney–Rivlin	16.7	6.7	0.4	23.4	$0.0 + 0.18$
Gent–Thomas	18.3	5.0	0.3	23.3	$0.0 + 0.24$
Carroll	17.6	5.7	0.3	23.3	$0.0 + 0.21$

principal elongation $\lambda > 1.5$, which we take as a bound of the small to moderate strain regime. We then determine the best fit values of the parameters C_1 and C_2 for each hyperelastic model and list them in table 1 together with the value of $\mathcal{E}$ for the chosen fit extent, which quantifies the quality of the fit. The sets of parameters describing our two distinct Ecoflex OO-30 samples are equivalent once normalized by the shear modulus μ_0; we give here and in the following only the parameters obtained by fitting the data of figure 2. We also represent the best fit curves in figure 4*a* and observe that all three models excellently capture the decrease in the Mooney plot. As already noted [9,48], the uniaxial extension test does not allow us to discriminate the form of the C_2 term.

We then compute the modified elasticity tensor $\boldsymbol{C}^0(\lambda, \lambda_3, \boldsymbol{p}, \omega, \beta')$ and obtain the dispersion relations of the three fundamental guided modes. To evidence the influence of imposed stretch, we compare the predicted dispersion relations to the data of figure 1 at a fixed frequency by representing the phase velocity parallel and perpendicular to the direction of imposed stretch as a function of λ for each mode (figure 4*c–f*). We choose an intermediate frequency for the in-plane modes, $f = 170$ Hz, where our measurements are the most reliable, and we choose $f = 50$ Hz for the out-of-plane mode as it is more sensitive to stretch in the long-wavelength regime. This choice of frequency is arbitrary, and we provide an interactive tool to explore the data and predictions at all frequencies [50]. Using this tool, we verify that the velocity of the A_0 mode parallel to the direction of elongation, for which most data lies in the long-wavelength limit, is independent of frequency and thus of the material's rheological behaviour and of β', as predicted by equation (3.19*a*). To perform a quantitative comparison between the measured and predicted values, we determine β' for each hyperelastic model by minimizing the relative error between the measured and predicted phase velocities of the SH_0 and S_0 modes at $f = 170$ Hz. The values of β' are listed in table 1 with uncertainty bounds corresponding to 95 % confidence intervals. Note that we enforce $\beta' \geq 0$ to ensure that the dynamic stress corresponds to dissipative incremental motions [36]. We find $\beta' = 0$ for all three models, in contrast with the non-zero value reported by Delory *et al.* [23], who considered larger values of λ in the fitting procedure. This suggests that viscous effects are not coupled to prestress in the small to moderate elongation regime (see equation (3.13)).

We represent the predicted phase velocities with solid lines in figure 4*c–f*, with shaded areas indicating 95 % confidence intervals stemming from the uncertainty on the value of β'. For the in-plane modes, the predictions are computed from the long-wavelength approximations of equations (3.15) and (3.16), while for the A_0 mode we use the long-wavelength prediction, equation (3.17*a*), parallel to the direction of elongation and the semi-analytical prediction in the perpendicular direction. First, the three models are able to qualitatively reproduce the measured phase velocities for all modes and propagation directions in the small to moderate strain regime. Moreover, the predictions for the SH_0 and A_0 modes in the direction $\boldsymbol{e}_1$, and to a lesser extent for the A_0 mode in direction $\boldsymbol{e}_3$, remain satisfying well outside the range of validity of these weakly nonlinear models. By contrast, we observe marked deviations at large stretch for the S_0 mode and for the SH_0 mode in the perpendicular direction. Second, unlike in the Mooney plot where all models fit the data equally well, the predicted phase velocities for the S_0 mode propagating perpendicular to the direction of imposed stretch (black triangles, figure 4*d*) significantly differ even when $\lambda < 1.5$, with the Mooney–Rivlin model capturing better the evolution of the phase

Downloaded from royalsocietypublishing.org/rspa/article-pdf/doi/10.1098/rspa.2026.0254/6169189/rspa.2026.0254.pdf
by guest
on 05 November 2026

velocity with λ. The shaded areas around the prediction lines for the perpendicular S_0 mode do not overlap at the end of the small to moderate elongation range, suggesting that the observed difference between the three models can be attributed to the form of the C_2 term rather than to the uncertainty in the determination of the parameter coupling viscoelasticity and hyperelasticity, although this remains to be confirmed by considering larger imposed elongations. The fact that the predictions differ can be qualitatively understood by considering the dependence of the phase velocities on W. For the shear horizontal and flexural modes, V is directly related to the stress in the sample, that is, to derivatives of W with the principal stretches (equations (3.18) and (3.19)), a quantity that all models fit equally well in the Mooney plot. By contrast, V depends on second-order derivatives of the strain energy density with the principal stretches for the pseudo-longitudinal mode, amplifying minute differences between the three models.

To summarize, in the small to moderate strain regime, all three hyperelastic models provide an excellent fit of the uniaxial extension data and satisfyingly capture the dispersion of guided waves propagating in the plate sample. Yet, we observe a small but significant difference between the predictions for pseudo-longitudinal waves propagating perpendicular to the direction of elongation. This piece of information allows us to discriminate the three models, that is, to obtain unique insight on the form of the I_2 contribution to the strain energy density. In the following, we tackle larger imposed elongations with the goal to identify if this trend persists.

(b) Strain-hardening regime

We move on to the strain-hardening regime, which corresponds to the upturn in the Mooney plot (figure 5*a*). Following the methodical approach of Destrade *et al.* [9], we add a power-law term to the previously considered hyperelastic models to account for strain hardening [51]:

$$W_I\left(I_1, I_2\right) = \frac{C_1}{2}\left(I_1 - 3\right) + C_2 f(I_2) + \frac{3^{1-N} C_3}{2N}\left(I_1^N - 3^N\right), \tag{4.5}$$

where C_3 and N are constants and $f\left(I_2\right)$ denotes the functional dependence of W on I_2 for the Mooney–Rivlin, Gent–Thomas and Carroll models. As λ increases, equation (4.5) indicates that W is proportional to $\lambda^{2(N-1)}$. This asymptotic behaviour corresponds to $\mathcal{M} \propto (1/\lambda)^{-2(N-1)}$, so that modelling the upturn in the Mooney plot requires $N > 1$.

We choose empirically the extent of the fit, $\lambda \in [1, 2.5]$, making sure that we consider values of λ large enough to capture the fact that $\mathcal{M}$ has gone through a minimum. Finding the set of parameters that best adjusts equation (4.5) to the simple elongation test is a nonlinear fitting procedure. In such a case, the outcome of the fit can be affected by the choice of initial conditions, with multiple local minima or even multiple minima with a similar level of error [21]. In order to remove the dependence on the initial guess, we vary N and perform a linear least-squares fit on the parameters C_1, C_2 and C_3 while recording the 2-norm of the relative residuals. The optimal set of parameters $\boldsymbol{p}$ is obtained for the value of N that minimizes this metric [9]. We plot the fits of the three hyperelastic models as solid lines in figure 5*a*. All models are in very good agreement with the data, as quantified by the maximal relative error $\mathcal{E}$ listed in table 2. Their fitted forms almost superimpose over the whole range of stretches $1 < \lambda < 2.5$, showing the importance of the added term to adjust the upturn of $\mathcal{M}$. Again, the Mooney plot alone is insufficient to discriminate between the models. We list in table 2 the associated set of parameters, and the value of the infinitesimal shear modulus for the three models described by equation (4.5). The obtained values of μ_0 are in very good agreement with those listed in table 1 for the small to moderate strain regime.

Moving to our elastic wave measurements, as in the small to moderate strain regime, we minimize the relative error between the predictions for the phase velocities of the in-plane modes, stemming from the fitted form of the strain energy densities (equation (4.5)), and the experimental measurements at fixed frequency to find the value of β' for each model. We list the obtained values in table 2 with uncertainty bounds corresponding to 95 % confidence intervals, and remark

Downloaded from royalsocietypublishing.org/rspa/article-pdf/doi/10.1098/rspa.2026.0254/6169189/rspa.2026.0254.pdf
by guest
on 05 November 2026

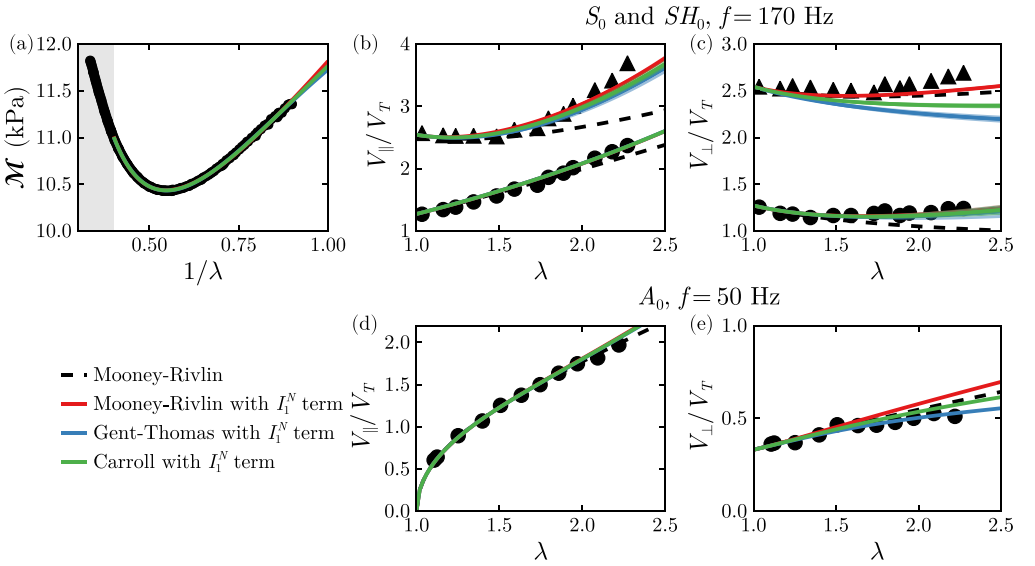


Figure 5. (a) Uniaxial elongation test for Ecoflex 00-30 represented in the Mooney space. The solid lines are the fits of equation (4.5) for $\lambda < 2.5$, when considering functional forms of the I_2 term corresponding to the Mooney–Rivlin, Gent–Thomas and Carroll models. (b-c) Normalized wave velocities for the SH_0 (dots) and S_0 (triangles) modes propagating parallel and perpendicular to the direction of elongation as a function of λ for $f = 170$ Hz. The solid lines are long-wavelength predictions computed from equations (3.15) and (3.16). The shaded area around the prediction lines corresponds to 95% confidence intervals resulting from the uncertainty on the value of β'. (d-e) Normalized wave velocities in the directions $\boldsymbol{e}_1$ and $\boldsymbol{e}_3$ for the A_0 mode. Parallel to the direction of propagation, the predictions come from the approximation equation (3.17*a*), while perpendicular to the direction of propagation we represent the results of the semi-analytical theory.

Table 2. Material parameters C_1, C_2, C_3 and N obtained by fitting the uniaxial extension data to equation (4.5) for $\lambda < 2.5$. The goodness of fit is quantified by the maximal relative error $\mathcal{E}$. We also list the values of the infinitesimal shear modulus $\mu_0 = C_1 + C_2 + C_3$, of β' and of the maximum of the relative errors between predicted and measured velocities across all modes and propagation directions $\mathcal{E}_V$.

model	C_1 (kPa)	C_2 (kPa)	C_3 (kPa)	N	$\mathcal{E}$(%)	μ_0 (kPa)	β'	$\mathcal{E}_V$(%)
MR $+I_1^N$	13.6	8.5	1.5	2.4	0.7	23.6	0.33 ± 0.06	25.5
GT $+I_1^N$	14.8	6.5	2.2	2.1	0.5	23.4	0.27 ± 0.11	16.7
C $+I_1^N$	14.2	7.4	2.0	2.2	0.6	23.5	0.29 ± 0.08	13.1

that they are now comparable to those given by Delory *et al.* [23]. When considering elongations beyond the small to moderate strain regime, viscoelasticity and prestress indeed become coupled. Importantly, the values of β' are all within their respective uncertainty bounds, indicating that the value is weakly affected by the choice of the constitutive law.

We compare the predicted phase velocities (solid lines with shaded areas representing 95 % confidence intervals stemming from the uncertainty in the determination of β') to the experimental data in figure 5*b–e*. Using the Mooney–Rivlin model predictions as a baseline (black dashed line), we immediately notice that overall the addition of the power-law term significantly improves the ability of the models to describe the experimental data at large λ and that the additional strain-hardening term has a similar influence on the behaviour of all three strain energy densities. Interestingly, unlike in the small to moderate strain regime, the deviations are not limited to the pseudo-longitudinal mode, which probes the derivatives of stress with stretch, but also appear

Downloaded from royalsocietypublishing.org/rspa/article-pdf/doi/10.1098/rspa.2026.0254/6169189/rspa.2026.0254.pdf
by guest
on 05 November 2026

for the flexural mode perpendicular to the direction of elongation. Qualitatively, the Mooney–Rivlin form of the C_2 term provides the best match to the variation of the phase velocity with λ for the S_0 mode, while the Gent–Thomas form provides the best agreement for the A_0 mode. The confidence intervals for the predicted phase velocities do not overlap for the S_0 and A_0 modes propagating perpendicular to the direction of imposed stretch. The uncertainty associated with the fit of β' does not explain the deviations between the predictions, confirming that they originate in the choice of the functional form of the C_2 term. Quantitatively, we choose to record the maximum of the relative errors between predicted and measured velocities across all modes and propagation directions, which we denote $\mathcal{E}_V$ (table 2). The Gent–Thomas and Carroll models perform very similarly and exhibit maximal error for the S_0 mode perpendicular to the direction of propagation. By contrast, the largest relative error for the Mooney–Rivlin predictions occurs for the out-of-plane mode in direction $\boldsymbol{e}_3$ with $\mathcal{E}_V = 25.5\,\%$. This behaviour can be understood by recalling that, in the long-wavelength limit, the velocity of the A_0 mode in direction $\boldsymbol{e}_3$ is related to the stress σ_3. Measuring the velocity of the flexural mode in the perpendicular direction thus highlights that we do not impose a true uniaxial deformation, that is, $\lambda_3 \neq 1/\sqrt{\lambda}$. The stress is biaxial, a deformation class for which the Mooney–Rivlin constitutive law is known to show large error in static tests [2], in agreement with our observations. Note that if we impose a strictly uniaxial deformation in our model, the predictions for the A_0 mode phase velocity in direction $\boldsymbol{e}_3$ collapse, but the deviations observed for the S_0 mode perpendicular to the direction of elongation are not affected. This demonstrates that the S_0 mode is intrinsically sensitive to the functional dependence of W on I_2 and that its discriminative power is not tied to non-ideal loading conditions. Ignoring the A_0 mode in the error calculation, we indeed find that the Mooney–Rivlin form of the C_2 term provides the lowest relative error with $\mathcal{E}_V = 5.7\,\%$.

The addition of a strain-hardening term to the Mooney–Rivlin, Gent–Thomas and Carroll models extends their ability to predict the dispersion of guided waves to the largest elongations investigated. As in the previous regime, comparing measured and predicted phase velocities for the three lowest-order guided modes allows one to distinguish constitutive laws that perform equivalently in the Mooney space. The data suggest that I_2 dependences of the Carroll or Gent–Thomas form perform equally well, while the Mooney–Rivlin form leads to a higher relative error for the out-of-plane mode perpendicular to the direction of elongation. However, adding a strain-hardening term comes at the expense of introducing two additional fit parameters. In the following, we explore whether simpler generalized neo-Hookean constitutive laws that allow us to describe the full simple tension curve, going beyond the upturn, with only three adjustable constants can also capture our dynamic measurements.

(c) Large deformation regime

We finally turn to hyperelastic models that allow us to describe the material behaviour over the whole range of imposed stretch. Modelling the stiffening that occurs in the large deformation regime requires one to identify the limiting behaviour of polymer chains, which is reflected in the singular behaviour of W at large λ. We consider two families of phenomenological strain energy density functions that mimic the large stretch behaviour of two different microscopical models. The Gent model [18]:

$$W_I\left(I_1, I_2\right) = -\frac{C_1 C_3}{2} \ln\left(1 - \frac{I_1 - 3}{C_3}\right) + C_2 f\left(I_2\right), \tag{4.6}$$

which represents the freely jointed chain model [17] and the Dobrynin & Carrillo model [52]:

$$W_I\left(I_1, I_2\right) = \frac{C_1}{6}\left(I_1 - 3 + \frac{2C_3}{1 - \left(I_1 - 3\right)/C_3} - 2C_3\right) + C_2 f\left(I_2\right), \tag{4.7}$$

Downloaded from royalsocietypublishing.org/rspa/article-pdf/doi/10.1098/rspa.2026.0254/6169189/rspa.2026.0254.pdf
by guest
on 05 November 2026

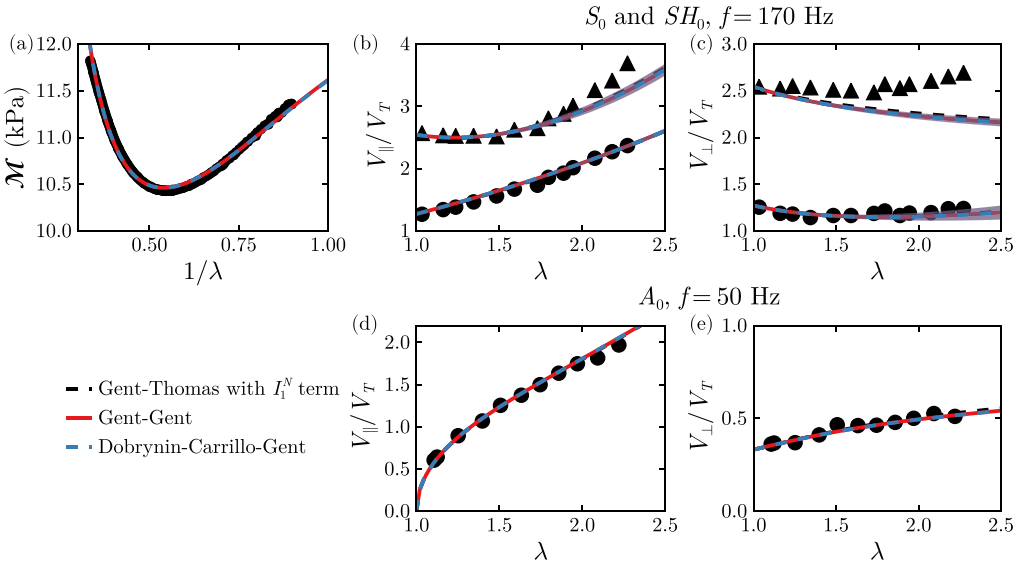


Figure 6. (a) Fits of the Gent model (solid line) and of the Dobrynin & Carrillo model (dashed line) augmented by a C_2 term of the Gent–Thomas form to the simple tension test for Ecoflex 00-30. (b-c) Normalized wave velocities for the SH_0 (dots) and S_0 (triangles) modes propagating parallel and perpendicular to the direction of elongation as a function of λ for $f = 170$ Hz. The lines are long-wavelength predictions computed from equations (3.15) and (3.16), and the shaded area corresponds to 95% confidence intervals resulting from the uncertainty on the value of β'. (d-e) Normalized wave velocities in the directions $\boldsymbol{e}_1$ and $\boldsymbol{e}_3$ for the flexural mode at $f = 50$ Hz. Parallel to the direction of propagation, the predictions come from the approximation equation (3.17*a*), while perpendicular to the direction of propagation we represent the results of the semi-analytical theory.

Table 3. Material parameters C_1, C_2 and C_3 obtained by fitting the uniaxial extension data to equations (4.6) and (4.7) using the Gent–Thomas form of $f\left(I_2\right)$. We quantify the goodness of fit through the maximal relative error $\mathcal{E}$, and list the values of the infinitesimal shear modulus $\mu_0 = C_1 + C_2$, and of β'.

model	C_1 (kPa)	C_2 (kPa)	C_3	$\mathcal{E}$ (%)	μ_0 (kPa)	β'
Gent–Gent	17.6	5.5	28.6	1.3	23.2	0.25 ± 0.12
Dobrynin–Carrillo–Gent	17.7	5.5	39.1	1.3	23.2	0.25 ± 0.12

which corresponds to the worm-like chain model [16]. Note that following the methodical approach of Destrade *et al.*, we complemented each generalized neo-Hookean model with a function of the second invariant that can take the Mooney–Rivlin, Gent–Thomas or Carroll form.

We focus on the micro-mechanically motivated Gent–Thomas form of the I_2-dependent term, as we identified that adding a stiffening contribution at large elongation has a similar effect on all models. As the fit procedure is nonlinear, we find the set of parameters $\boldsymbol{p}$ that best describes the uniaxial extension data using a genetic algorithm [28], which we initialize with the values of C_1 and C_2 listed in table 1 for the Gent–Thomas model, and with $C_3 = 10$. The values of the three constants are listed in table 3, and we plot the fits of equations (4.6) and (4.7) to the simple extension test in figure 6*a*. The fitted forms of W excellently describe the data in the Mooney space over the whole range of imposed stretch, and we recover a value of the infinitesimal shear modulus in agreement with that previously obtained. The two three-parameter models (equations (4.6) and (4.7)) allow us to describe the whole stress–strain curve with only a slight increase in maximal relative error $\mathcal{E}$ compared to the four-parameter models used in the previous section.

We compute the modified elasticity tensor $\mathbf{C}^0\left(\lambda, \lambda_3, \boldsymbol{p}, \omega, \beta'\right)$, allowing us to access the dispersion relations of guided waves propagating in the plate. We list the value of β' with uncertainty bounds

Downloaded from royalsocietypublishing.org/rspa/article-pdf/doi/10.1098/rspa.2026.0254/6169189/rspa.2026.0254.pdf
by guest
on 05 November 2026

corresponding to 95 % confidence intervals determined by minimizing the relative error between the measurement and predictions for the phase velocities of the in-plane modes at $f = 170$ Hz in table 3 and represent the predictions in figure 6*b–e* (solid red line and blue dashed line with shaded areas corresponding to 95 % confidence intervals coming from the uncertainty on β'). First, the forms of W introduced in equations (4.6) and (4.7) enable us to accurately predict all phase velocities for all values of λ probed in this study and perform equivalently as the Gent–Thomas model augmented by an I_1^N term (black dashed line). Second, the phase velocities deduced from both models are indistinguishable for all three fundamental modes propagating in directions $\boldsymbol{e}_1$ and $\boldsymbol{e}_3$. We verified that this collapse persists in the limiting extension regime by plotting the predictions up to $\lambda = 4$, although we do not access such large extensions experimentally. We stress that, if we wanted to favour the agreement for the S_0 in-plane mode, we could have chosen to use the Mooney–Rivlin form of the C_2 term to augment both limiting-chain constitutive laws, without affecting the above observations (see the interactive tool [50]).

The Gent–Gent [53] and Dobrynin & Carrillo [52] models complemented by a function of the second invariant allow us to describe the uniaxial extension test and the propagation of guided waves over the entire range of imposed elongation. Both models perform equivalently in static and dynamic measurements: we are not able to discriminate the behaviour of polymer chains at large extension. We emphasize that the Gent–Gent and Dobrynin & Carrillo models capture the material's behaviour in all stretch regimes using only three material parameters. In that light, the two families of strain energy density functions introduced in this subsection can advantageously replace the four-parameter models used to describe strain-hardening in the previous section.

5. Conclusion

In this work, we measure the dispersion relation of the three zero-order guided modes propagating in a plate undergoing uniaxial extension, both parallel and perpendicular to the direction of imposed stretch. Combining the material's rheological behaviour with the acoustoelastic theory, we show that these dynamic measurements give access to pieces of information that cannot be obtained from the stress–strain curve recorded in corresponding simple tension tests. Indeed, the pseudo-longitudinal mode is sensitive to second derivatives of the strain energy density with stretch and, in the long-wavelength limit, the flexural mode propagating perpendicular to the direction of elongation is sensitive to the stress in the same direction, evidencing deviations from a purely uniaxial stress state. This additional insight comes at the expense of introducing an extra fit parameter which couples the viscoelastic and hyperelastic behaviour of our sample.

Using the methodical approach introduced by Destrade *et al.* [9], we demonstrate by analysing data in the small to moderate strain and in the strain-hardening regimes that guided wave measurements enable us to discriminate constitutive laws with different functional dependence on I_2 that fit equally well the static curve. Although we presented results at fixed frequency, this discriminative capability is not tied to the frequency choice (see the interactive tool [50]). We find that the Gent–Thomas and Carroll forms of the C_2 term perform comparably well, and overall provide a better description of the whole dataset than the Mooney–Rivlin form. However, we remark that if we had imposed a purely uniaxial deformation, the Mooney–Rivlin model would provide the best predictions, and emphasize that the sensitivity of the pseudo-longitudinal mode to the functional dependence on I_2 persists in these idealized loading conditions. By contrast, the dynamic data do not enable us to tell apart the predictions from generalized neo-Hookean models that empirically represent distinct singular strain energy density behaviour in the limiting-chain regime. We also note that viscous effects and prestress begin to interact only when considering elongations beyond the small to moderate strain regime and that the value of the coupling parameter is weakly affected by the choice of constitutive law.

These findings echo the insight gained by performing static experiments across multiple deformation classes. The Mooney–Rivlin form of the C_2 term gives the best predictions except when

Downloaded from royalsocietypublishing.org/rspa/article-pdf/doi/10.1098/rspa.2026.0254/6169189/rspa.2026.0254.pdf
by guest
on 05 November 2026

considering the flexural mode propagating perpendicular to the imposed elongation, that is, when our experiments are sensitive to the presence of a small biaxial stress. This observation corroborates that of Treloar [2], who evidenced that the Mooney–Rivlin model fits excellently uniaxial data, but gives large errors in equibiaxial or compression tests. For the A_0 mode, the Gent–Thomas form of the C_2 term provides the best agreement, consistent with the findings of Ogden *et al.* [21], who showed that the Gent–Gent model fitted on uniaxial data performs satisfyingly across a variety of deformation classes.

In conclusion, our results show that a constitutive law combining a generalized neo-Hookean term with an I_2-dependent Gent–Thomas or Carroll contribution, such as the Gent–Gent model [53], provides a consistent description of both simple tension tests and incremental wave propagation, with low relative error. More generally, guided-wave measurements in a plate under uniaxial extension reveal constitutive modelling differences that are indistinguishable at the level of the stress–strain curve. The three-dimensional wave fields we measure hold more information than the underlying static simple tension test, providing a new tool to discriminate constitutive laws when having access to a single deformation class. Yet, the insight gained through our measurements does not alleviate the need to perform additional mechanical tests. Equibiaxial extension, compression or simple shear tests reveal pieces of information on the choice of the I_2 term [2,9] that are distinct from and complementary to those obtained in our measurements under idealized loading conditions.

This observation leads us to the first natural extension of this work: performing incremental guided wave measurements under other underlying static deformations and identifying the corresponding insight on the form of the material constitutive law. Second, exploiting higher-order guided modes would allow the extraction of richer information from dispersion measurements. This could be achieved, for instance, by replacing the plate geometry considered here with a strip geometry, which supports a larger number of guided modes within the same frequency range [33]. Beyond dispersion, measuring wave attenuation may provide additional insight into the multiple choices for modelling viscoelasticity discussed by Berjamin & Destrade [37] and into the coupling between hyperelastic and viscoelastic effects. In the present study, only the first-order term coupling the hyperelastic and viscous response is considered (see equation (3.12)), an approximation that may become inaccurate at large elongations, where the constitutive response is strongly nonlinear. Third, developing a wave-based inversion procedure to obtain the constitutive law's adjustable parameters directly from the dynamic data remains a challenge. We outline below our vision of the next steps to be taken towards this goal. (i) The experimental and signal-processing methods need to be refined to extract accurately the complex wavenumber, capturing both dispersion and attenuation, across the widest possible frequency range. This can be achieved by utilizing high-resolution methods, such as the ESPRIT algorithm [54], to isolate overlapping guided modes and decay rates. (ii) A multi-frequency inversion framework is required to aggregate dispersion and attenuation data across all measured frequencies. (iii) A methodical fitting procedure must be developed, similarly to the static case, to address the ill-conditioning that arises when simultaneously optimizing multiple hyperelastic parameters [21]. For dynamic measurements, this also concerns the viscoelastic parameters, τ and n, and the parameter-coupling viscoelasticity and hyperelasticity, β', possibly leading to additional issues compared to the static case. Regarding the constitutive law constants, the wave-based inversion could exploit model-independent combinations of guided mode velocities that relate directly to the principal stress state (see §2), enabling us to use the procedure of Destrade *et al.* [9]. Simultaneous wave propagation and principal stress measurements using such observables would also allow us to quantify stress relaxation, an effect we neglected in this work.

Finally, we discuss how our guided wave measurements compare to elastography, a popular dynamic stiffness measurement technique based on monitoring the propagation of bulk shear waves using ultrasound imaging, magnetic resonance imaging or optical coherence tomography [55]. The dispersion of bulk shear waves holds similar information to that probed in our measurements [56–58]. We only note that bulk shear waves propagating on a principal axis do not give access to second-order derivatives of the strain energy density, unlike the S_0 mode, an

Downloaded from royalsocietypublishing.org/rspa/article-pdf/doi/10.1098/rspa.2026.0254/6169189/rspa.2026.0254.pdf
by guest
on 05 November 2026

effect that originates from mode conversion at the interfaces of the guiding geometry. A similar mode conversion is expected to occur near crack tips, as investigated in [59]. More generally, taking guiding into account allows us to extend the scope of stiffness measurements to situations where boundaries prevent the observation of bulk wave propagation, which could be of interest for imaging in biological tissues such as tendons [60]. Overall, all these perspectives suggest that incremental guided wave propagation may become a powerful tool for the mechanical characterization of soft materials.

Data accessibility. The data associated with this article and the interactive visualization tool are openly available on Zenodo [50].

Declaration of AI use. We have not used AI-assisted technologies in creating this article.

Authors' contributions. P.C.: conceptualization, investigation, software, writing—original draft, writing—review and editing; S.C.: investigation, writing—review and editing; F.L.: conceptualization, funding acquisition, investigation, supervision, validation, writing—review and editing.

All authors gave final approval for publication and agreed to be held accountable for the work performed therein.

Conflict of interest declaration. We declare we have no competing interests.

Funding. We acknowledge funding by the Agence Nationale de la Recherche (ANR), grant ANR-24-CE30-3540. This work has received support under the program "Investissements d'Avenir" launched by the French Government.

Acknowledgements. We thank Florent Dorlot and Simon Yves for their help in setting up the experiments and Alexandre Delory for insightful discussions.

References

1. Beatty MF. 1987 Topics in finite elasticity: hyperelasticity of rubber, elastomers, and biological tissues—with examples. *Appl. Mech. Rev.* **40**, 1699–1734. (doi:10.1115/1.3149545)
2. Treloar LRG. 2005 *The physics of rubber elasticity*. Oxford, UK: Oxford University Press. (doi:10.1093/oso/9780 198570271.001.0001)
3. Goriely A, Ben Amar M. 2005 Differential growth and instability in elastic shells. *Phys. Rev. Lett.* **94**, 198103. (doi:10.1103/physrevlett.94.198103)
4. Holzapfel GA, Ogden RW. 2010 Constitutive modelling of arteries. *Proc. R. Soc. A* **466**, 1551–1597. (doi:10.1098/rspa.2010.0058)
5. Laschi C, Mazzolai B, Cianchetti M. 2016 Soft robotics: Technologies and systems pushing the boundaries of robot abilities. *Sci. Rob.* **1**, eaah3690. (doi:10.1126/scirobotics.aah3690)
6. Ng CSX, Tan MWM, Xu C, Yang Z, Lee PS, Lum GZ. 2021 Locomotion of miniature soft robots. *Adv. Mat.* **33**, 2003558. (doi:10.1002/adma.202003558)
7. Mondal S, Das S, Nandi AK. 2020 A review on recent advances in polymer and peptide hydrogels. *Soft Matter* **16**, 1404–1454. (doi:10.1039/c9sm02127b)
8. Li M, Tang Y, Soon RH, Dong B, Hu W, Sitti M. 2022 Miniature coiled artificial muscle for wireless soft medical devices. *Sci. Adv.* **8**, eabm5616. (doi:10.1126/sciadv.abm5616)
9. Destrade M, Saccomandi G, Sgura I. 2017 Methodical fitting for mathematical models of rubber-like materials. *Proc. R. Soc. A: Math. Phys. Eng. Sci* **473**, 20160811. (doi:10.1098/rspa.2016.0811)
10. Treloar LRG. 1944 Stress-strain data for vulcanized rubber under various types of deformation. *Trans. Faraday Soc.* **40**, 59–70. (doi:10.1039/tf9444000059)
11. Wang MC, Guth E. 1952 Statistical theory of networks of non-gaussian flexible chains. *J. Chem. Phys.* **20**, 1144–1157. (doi:10.1063/1.1700682)
12. Arruda EM, Boyce MC. 1993 A three-dimensional constitutive model for the large stretch behavior of rubber elastic materials. *J. Mech. Phys. Solids* **41**, 389–412. (doi:10.1016/0022-5096(93)90013-6)
13. Mooney M. 1940 A theory of large elastic deformation. *J. Appl. Phys.* **11**, 582–592. (doi:10.1063/1.1712836)
14. Rivlin RS. 1948 Large elastic deformations of isotropic materials IV. Further developments of the general theory. *Philos. Trans. R. Soc. London. Ser. A* **241**, 379–397. (doi:10.1098/rsta.1948.0024)

Downloaded from royalsocietypublishing.org/rspa/article-pdf/doi/10.1098/rspa.2026.0254/6169189/rspa.2026.0254.pdf
by guest
on 05 November 2026

15. Ogden RW. 1972 Large deformation isotropic elasticity–on the correlation of theory and experiment for incompressible rubberlike solids. *Proc. R. Soc. Lond. A* **326**, 565–584. (doi:10.1098/rspa.1972.0026)
16. Puglisi G, Saccomandi G. 2016 Multi-scale modelling of rubber-like materials and soft tissues: an appraisal. *Proc. R. Soc. A* **472**, 20160060. (doi:10.1098/rspa.2016.0060)
17. Horgan CO, Saccomandi G. 2002 A molecular-statistical basis for the Gent constitutive model of rubber elasticity. *J. Elast.* **68**, 167–176. (doi:10.1023/a:1026029111723)
18. Gent AN. 1996 A new constitutive relation for rubber. *Rubber Chem. Technol.* **69**, 59–61. (doi:10.5254/1.3538357)
19. Kroon M. 2011 An 8-chain model for rubber-like materials accounting for non-affine chain deformations and topological constraints. *J. Elast.* **102**, 99–116. (doi:10.1007/s10659-010-9264-7)
20. Gent AN, Thomas AG. 1958 Forms for the stored (strain) energy function for vulcanized rubber. *J. Polym. Sci.* **28**, 625–628. (doi:10.1002/pol.1958.1202811814)
21. Ogden RW, Saccomandi G, Sgura I. 2004 Fitting hyperelastic models to experimental data. *Comput. Mech.* **34**, 484–502. (doi:10.1007/s00466-004-0593-y)
22. Royer D, Dieulesaint E. 1999 *Elastic waves in solids I: free and guided propagation*. Berlin: Springer Science & Business Media.
23. Delory A, Lemoult F, Eddi A, Prada C. 2023 Guided elastic waves in a highly-stretched soft plate. *Extreme Mech. Lett.* **61**, 102018. (doi:10.1016/j.eml.2023.102018)
24. Delory A, Lemoult F, Lanoy M, Eddi A, Prada C. 2022 Soft elastomers: a playground for guided waves. *J. Acoust. Soc. Am.* **151**, 3343–3358. (doi:10.1121/10.0011391)
25. Laurent J, Royer D, Prada C. 2020 In-plane backward and zero group velocity guided modes in rigid and soft strips. *J. Acoust. Soc. Am.* **147**, 1302–1310. (doi:10.1121/10.0000760)
26. Horgan CO, Saccomandi G. 2004 Constitutive models for compressible nonlinearly elastic materials with limiting chain extensibility. *J. Elast.* **77**, 123–138. (doi:10.1007/s10659-005-4408-x)
27. Norris AN. 2024 Finite-amplitude waves in solids. In *Nonlinear acoustics*, pp. 259–273. Cham: Springer Nature Switzerland.
28. Hansen N. 2016 The CMA evolution strategy: a tutorial. *arXiv preprint arXiv:1604.00772*.
29. Ogden RW. 1997 *Non-linear elastic deformations*. New York: Dover Publications. (doi:10.1016/0264-682x(84)90061-3)
30. Destrade M, Saccomandi G. 2007 *Waves in nonlinear pre-stressed materials*. Vienna: Springer Vienna. (doi:10.1007/978-3-211-73572-5)
31. Yasar TK, Royston TJ, Magin RL. 2013 Wideband MR elastography for viscoelasticity model identification. *Magn. Reson. Med.* **70**, 479–489. (doi:10.1002/mrm.24495)
32. Liu Y, Yasar TK, Royston TJ. 2014 Ultra wideband (0.5–16 kHz) MR elastography for robust shear viscoelasticity model identification. *Phys. Med. Biol.* **59**, 7717.
33. Lanoy M, Lemoult F, Eddi A, Prada C. 2020 Dirac cones and chiral selection of elastic waves in a soft strip. *Proc. Natl Acad. Sci. USA* **117**, 30186–30190. (doi:10.1073/pnas.2010812117)
34. Winter HH, Chambon F. 1986 Analysis of linear viscoelasticity of a crosslinking polymer at the gel point. *J. Rheol.* **30**, 367–382. (doi:10.1122/1.549853)
35. Long D, Ajdari A, Leibler L. 1996 Static and dynamic wetting properties of thin rubber films. *Langmuir* **12**, 5221–5230. (doi:10.1021/la9604700)
36. Destrade M, Ogden RW, Saccomandi G. 2009 Small amplitude waves and stability for a pre-stressed viscoelastic solid. *Z. Angew. Math. Phys.* **60**, 511–528. (doi:10.1007/s00033-008-7147-6)
37. Berjamin H, Destrade M. 2025 Models of fractional viscous stresses for incompressible materials. *Math. Mech. Solids* **30**, 540–555. (doi:10.1177/10812865241233973)
38. Delory A, Kiefer DA, Lanoy M, Eddi A, Prada C, Lemoult F. 2024 Viscoelastic dynamics of a soft strip subject to a large deformation. *Soft Matter* **20**, 1983–1995. (doi:10.1039/d3sm01485a)
39. Kiefer DA, Delory A, Lemoult F. 2024 GEW soft strip. Zenodo. (doi:10.5281/zenodo.10641373)
40. Rogerson GA, Prikazchikova LA. 2009 Generalisations of long wave theories for pre-stressed compressible elastic plates. *Int. J. Non-Linear Mech.* **44**, 520–529. (doi:10.1016/j.ijnonlinmec.2008.11.002)
41. Li GY, Gower AL, Destrade M, Yun SH. 2022 Non-destructive mapping of stress and strain in soft thin films through sound waves. *Commun. Phys.* **5**, 231. (doi:10.1038/s42005-022-01000-3)
42. Zhang Z, Li GY, Jiang Y, Zheng Y, Gower AL, Destrade M, Cao Y. 2023 Noninvasive measurement of local stress inside soft materials with programmed shear waves. *Sci. Adv.* **9**, eadd4082. (doi:10.1126/sciadv.add4082)

Downloaded from royalsocietypublishing.org/rspa/article-pdf/doi/10.1098/rspa.2026.0254/6169189/rspa.2026.0254.pdf
by guest
on 05 November 2026

43. Adamou A, Craster RV. 2004 Spectral methods for modelling guided waves in elastic media. *J. Acoust. Soc. Am.* **116**, 1524–1535. (doi:10.1121/1.1777871)
44. Shen J, Tang T, Wang L. 2011 *Spectral methods: algorithms, analysis and applications*. Springer Series in Computational Mathematics, vol. 41. Berlin: Springer Science & Business Media. (doi:10.1007/978-3-540-71041-7)
45. Kiefer DA. 2022 *Elastodynamic quasi-guided waves for transit-time ultrasonic flow metering*, pp. 955–959. Erlangen: FAU University Press. (doi:10.1121/1.389841)
46. Kiefer DA. 2024 GEW dispersion script. Zenodo. (doi:10.5281/zenodo.7010603)
47. Chantelot P. 2026 POnG.jl. Zenodo. (doi:10.5281/zenodo.19069061)
48. Carroll MM. 2011 A strain energy function for vulcanized rubbers. *J. Elast.* **103**, 173–187. (doi:10.1007/s10659-010-9279-0)
49. Anssari-Benam A, Bucchi A, Destrade M, Saccomandi G. 2022 The generalised Mooney space for modelling the response of rubber-like materials. *J. Elast.* **151**, 127–141. (doi:10.1007/s10659-022-09889-1)
50. Chantelot P, Croquette S, Lemoult F. (2026). Guided elastic waves informed material modelling of soft incompressible media: data and interactive visualization tool [Data set]. Zenodo. (doi:10.5281/zenodo.19108690)
51. Lopez-Pamies O. 2010 A new I1-based hyperelastic model for rubber elastic materials. *C. R. Méc.* **338**, 3–11. (doi:10.1016/j.crme.2009.12.007)
52. Dobrynin AV, Carrillo JMY. 2011 Universality in nonlinear elasticity of biological and polymeric networks and gels. *Macromolecules* **44**, 140–146. (doi:10.1021/ma102154u)
53. Pucci E, Saccomandi G. 2002 A note on the Gent model for rubber-like materials. *Rubber Chem. Technol.* **75**, 839–852. (doi:10.5254/1.3547687)
54. Margerit P, Lebée A, Caron JF, Boutillon X. 2018 High resolution wavenumber analysis (HRWA) for the mechanical characterisation of viscoelastic beams. *J. Sound Vib.* **433**, 198–211. (doi:10.1016/j.jsv.2018.06.062)
55. Ormachea J, Parker KJ. 2020 Elastography imaging: the 30 year perspective. *Phys. Med. Biol.* **65**, 24TR06. (doi:10.1088/1361-6560/abca00)
56. Ogden R, Sotiropoulos D. 1997 The effect of pre-stress on the propagation and reflection of plane waves in incompressible elastic solids. *IMA J. Appl. Math.* **59**, 95–121. (doi:10.1093/imamat/59.1.95)
57. Gennisson JL, Rénier M, Catheline S, Barrière C, Bercoff J, Tanter M, Fink M. 2007 Acoustoelasticity in soft solids: Assessment of the nonlinear shear modulus with the acoustic radiation force. *J. Acoust. Soc. Am.* **122**, 3211–3219. (doi:10.1121/1.2793605)
58. Jiang Y, Li G, Qian LX, Liang S, Destrade M, Cao Y. 2015 Measuring the linear and nonlinear elastic properties of brain tissue with shear waves and inverse analysis. *Biomech. Model. Mechanobiol.* **14**, 1119–1128. (doi:10.1007/s10237-015-0658-0)
59. Le Blay H, Deffieux T, Laiarinandrasana L, Tanter M, Marcellan A. 2024 Stress amplification and relaxation imaging around cracks in nanocomposite gels using ultrasound elastography. *Soft Matter* **20**, 9127–9139. (doi:10.1039/d4sm00909f)
60. Croquette S, Delory A, Kiefer DA, Prada C, Lemoult F. 2025 Exploring the limits to quantitative elastography: supersonic shear imaging in stretched soft strips. *Phys. Med. Biol.* **70**, 145009. (doi:10.1088/1361-6560/adea2a)

Downloaded from royalsocietypublishing.org/rspa/article-pdf/doi/10.1098/rspa.2026.0254/6169189/rspa.2026.0254.pdf
by guest
on 05 November 2026